Chinese Chemical Letters 37 (2026) 111110

Contents lists available at ScienceDirect

Chinese Chemical Letters

journal homepage: www.elsevier.com/locate/cclet

Constructing stable cathode by g-C_3N_4 nanosheets for high-energy all-solid-state lithium-sulfur batteries

Ying Li[a], Ze-Chen Lv[a,b], Peng-Fei Wang[a,b,*], Jie Shu[c], Ping He[d,*], Ting-Feng Yi[a,b,*]

[a] School of Materials Science and Engineering, Northeastern University, Shenyang 110819, China
[b] Key Laboratory of Dielectric and Electrolyte Functional Material Hebei Province, School of Resources and Materials, Northeastern University at Qinhuangdao, Qinhuangdao 066004, China
[c] School of Materials Science and Chemical Engineering, Ningbo University, Ningbo 315211, China
[d] Center of Energy Storage Materials & Technology, College of Engineering and Applied Sciences, Jiangsu Key Laboratory of Artificial Functional Materials, National Laboratory of Solid State Microstructures and Collaborative Innovation Center of Advanced Microstructures, Nanjing University, Nanjing 210093, China

ARTICLE INFO

Article history:
Received 3 January 2025
Revised 11 March 2025
Accepted 18 March 2025
Available online 18 March 2025

Keywords:
Polyethylene oxide
All-solid-state electrolyte
Lithium-sulfur battery
Adsorption and catalysis
Coulombic efficiency

ABSTRACT

Poly(ethylene oxide)-based polymer all-solid-state lithium-sulfur batteries (ASSLSBs) have been a prominent direction in new generation of energy storage devices due to their safety, low cost and high specific energy. However, the performance degradation arising from the "shuttle effect" and poor ion transport dynamics limit its further development. Herein, for the first time, we introduce the concepts of adsorption and catalysis into polymer ASSLSBs. By combining S@KB with g-C_3N_4, the polysulfides shuttling is significantly inhibited. Meanwhile, the kinetic process of the cathode is obviously improved, which is confirmed by *in situ* electrochemical impedance spectroscopy. The battery with g-C_3N_4 can provide a high reversible capacity 1078.5 mAh/g, and can be stabilized for 150 cycles with a final Coulombic efficiency of 97.47 %, implying a superior electrochemical stability than previously reported. Furthermore, the intrinsic mechanisms of adsorption and catalysis are intensively studied by means of XPS, DFT calculations, and galvanostatic intermittent titration technique. Changes in electrode properties before and after cycling have also been used to study battery stability. Overall, this work will open the door to the novel polymer all-solid-state lithium-sulfur battery design for practical realization of high-energy batteries.

© 2026 Published by Elsevier B.V. on behalf of Chinese Chemical Society and Institute of Materia Medica, Chinese Academy of Medical Sciences.

The ever-increasing requirement for high-energy-density battery of electric vehicles, portable devices and large-scale energy storage grids has attracted a lot of attention beyond state-of-the-art commercial lithium-ion battery system [1–3]. Solid-state lithium-sulfur batteries [4], which occupy the dual advantages of lithium-sulfur batteries (high capacity [5] and high specific energy [6]) and solid-state batteries (high energy [7,8] and high safety [9]), has been a prominent direction in a new generation of energy storage devices. Regarding the selection of solid electrolyte, two categories including inorganic and polymer are extensively studied [10,11]. Inorganic electrolyte owns high ionic conductivity, but interface problems and high cost are the key factors restricting its application [12]. By contrast, polymer-based solid-state electrolytes offer advantages such as excellent processability, close electrode contact, non-toxicity, and low cost [13], making them poised for early commercialization. Of these, polyethylene oxide (PEO) stands out as an electrolyte matrix with ether oxygen bonds as its main chain, exhibiting good compatibility with sulfur cathodes [12]. PEO also serves as an excellent Li^+ complexing agent with strong Li^+ dissolution capabilities, thus demonstrating significant potential for various applications [14].

Notwithstanding, PEO-based all-solid-state lithium-sulfur battery (ASSLSB) is beset by some key scientific questions. Firstly, because the reaction mechanism in the PEO-based electrolyte is similar to the "dissolution and deposition" in the liquid electrolyte [15,16], the battery exhibits a serious "shuttle effect", which results in low utilization of active substances and short cycling life. Secondly, on the anode side, the shuttling polysulfides will react with metal Li to form an unstable solid electrolyte interphase (SEI) film [17], leading to a continuous consumption of electrode materials. Thirdly, the electrolyte does not possess sufficient ionic conductivity ($\sim 10^{-6}$ S/cm) due to the highly crystalline of PEO (75 %–80 %) at room temperature, resulting a lower battery capacity value [11]. The nature of the first two issues is caused by the "shuttle effect",

* Corresponding authors.
E-mail addresses: wangpengfei@neuq.edu.cn (P.-F. Wang), pinghe@nju.edu.cn (P. He), tfyihit@163.com (T.-F. Yi).

https://doi.org/10.1016/j.cclet.2025.111110
1001-8417/© 2026 Published by Elsevier B.V. on behalf of Chinese Chemical Society and Institute of Materia Medica, Chinese Academy of Medical Sciences.

and the third issue is due to the characteristics of the electrolyte itself. Therefore, seeking a suitable way to solve the above issues is the key to this battery system.

Employing fillers to construct PEO-based polymer composite solid electrolytes is a common approach [18]. The abundant functional groups on the filler surface can change the internal chemical environment of the electrolyte, thus improving the ionic conductivity. Meanwhile, these fillers can inhibit the shuttle of polysulfides by blocking effect. Lee *et al.* [19] incorporated nano TiO_2 into PEO-based electrolytes, where the Lewis acidic groups on the transition metal oxide surfaces interacted with the Lewis basic units in PEO, resulting in reduced crystallinity of PEO and enhanced ionic conductivity [20]. Besides the above inert fillers, there is also an active filler, which can decrease the crystallinity and further improve the conductivity by conducting Li^+ on its own. Tao *et al.* [21] utilized garnet-type active $Li_7La_3Zr_2O_{12}$ as a filler, enabling the PEO-based electrolyte to achieve an ionic conductivity of 1.1×10^{-4} S/cm at 40 °C. Moreover, lithium-sulfur batteries based on this electrolyte provided a capacity exceeding 900 mAh/g at 37 °C.

Another common approach is to replace part of the functional groups of the lithium salt $LiN(CF_3SO_2)_2$ (LiTFSI), and then construct a dense and stable SEI film with high ionic conductivity to enhance the stability of the battery [22]. Eshetu *et al.* [23] utilized -SO_2F substitution for -SO_2CF_3 in LiTFSI and applied it in PEO-based ASSLSBs. The SEI film of this system consists of a balanced organic-inorganic composition, which can prevent polysulfides from reacting with the lithium metal anode, resulting in a high capacity of 1392 mAh/g. Zhang *et al.* [24] replaced one -F with -H in LiTFSI, where the asymmetric structure and electrochemically unstable -CF_2H easily decompose on the lithium surface, forming a dense SEI containing the ion conductor LiH, inhibiting the reaction between polysulfides and lithium, and to some extent enhancing the ion conductivity. Thus, the battery can achieve a capacity of 1035 mAh/g. However, modifying the functional groups in lithium salts primarily targets the "shuttle effect" of batteries, with limited enhancement in the ion conductivity of the electrolyte itself.

Indeed, besides the modification of the electrolyte itself, the ingenious design on the cathode side is equally critical but scarcely reported in polymer-based solid-state lithium-sulfur batteries. Herein, for the first time, we introduce the concepts of adsorption and catalysis into polymer ASSLSBs. By combining S@KB with g-C_3N_4, the kinetic process of the positive electrode is obviously improved. g-C_3N_4 is a two-dimensional lamellar material with strong covalent bonds between its conjugated layers [25], which are connected by tertiary amines [26], so it has high chemical and thermal stability. Moreover, lone pair electrons on the N atoms can provide an active site [27], adsorb and catalyze the conversion of polysulfides. Finally, the "shuttle effect" is effectively inhibited, and the dynamic process of the battery is greatly improved, which makes up for the low ionic conductivity of the polymer-based electrolyte to a certain extent.

Fig. 1 exhibits the preparation and related spectral characterization of electrode materials. Firstly, the specific preparation steps of the electrode material, including the respective sintering and physical mixing processes, was detailed in Supporting information. Then a schematic diagram for the action mechanism of g-C_3N_4 is displayed (Fig. 1a), involving the adsorption and catalysis process. The samples can be named S/KB and S/KB-CN1 (3 wt%), S/KB-CN2 (5 wt%), S/KB-CN3 (8 wt%), in that order, depending on the amount of added g-C_3N_4. The sulfur content was confirmed to be 65 % for S/KB-CN2 by thermogravimetric test (Fig. S1 in Supporting information). In order to deeply investigate the crystal structures of S/KB, g-C_3N_4 and S/KB-CN2, these materials were tested by X-ray diffraction (XRD, Fig. 1b). The diffraction peaks of the S/KB composites correspond to the standard card (PDF #78–1889) and the crystal structure is consistent with the rhombohedral structure of

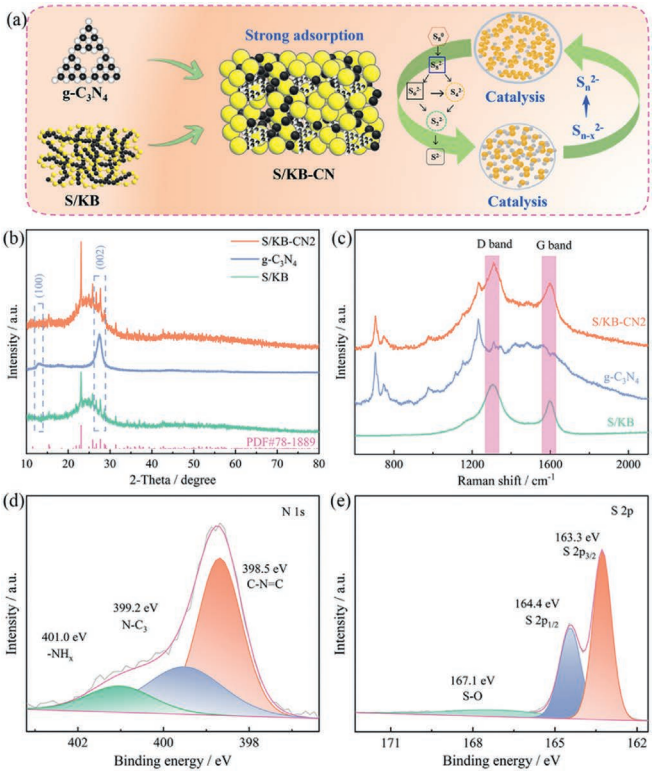


Fig. 1. Preparation and related spectral characterization of materials. (a) The preparation process of electrode material (S/KB/g-C_3N_4, abbreviated as S/KB-CN) and its action mechanism in battery. (b) XRD and (c) Raman spectra of S/KB, g-C_3N_4 and S/KB-CN2 materials. XPS spectra of (d) N 1s and (e) S 2p for S/KB-CN2 materials.

sulfur [28]. Subsequently, the Raman results (Fig. 1c) shows that the I_D/I_G value of S/KB-CN2 (1.516) is greater than that of S/KB (1.439), indicating that the defects of the material increased after the introduction of g-C_3N_4. The increased defects are favorable for the adsorption of polysulfides, which improves the reactivity of the electrode material. In addition, the characteristic peaks belonging to g-C_3N_4 clearly appear in the range of $<1000\,cm^{-1}$, which further confirms that g-C_3N_4 has been successfully complexed with S/KB.

Next, the chemical properties of the S/KB-CN2 composites were analyzed by XPS tests and the results are shown in Fig. S2 (Supporting information) and Figs. 1d and e. The XPS gross spectrum (Fig. S2a) of the S/KB-CN2 confirms the presence of the elements sulfur (S 2p), carbon (C 1s) and nitrogen (N 1s) in the material, which correspond to the different chemical states of these elements. Fig. S2b illustrates the high-resolution XPS pattern of C 1s and its fitting results. The peak of 283.8 eV can be ascribed to the C-C of the indeterminate source carbon in KB. The XPS peak of 284.5 eV is related to the C-O bond, while the peak at 288.1 eV can correspond to the N-C_3 correlation formed by combining C atoms and N atoms in the g-C_3N_4 lattice, which is slightly shifted in peak position compared to the g-C_3N_4 XPS pattern. Then the XPS peaks and the fitting results in three fine peaks of N 1s are shown in Fig. 1d. The peak at 398.5 eV corresponds to the C-N=C bond, while the peaks at 399.2 eV and 401.0 eV correspond to the N-C_3 and -NH_x bonds, respectively. The S 2p peak (Fig. 1e) induced by spin-orbit splitting splits into a double peak of S $2p_{1/2}$ at 164.4 eV and S $2p_{3/2}$ at 163.3 eV, with an intensity ratio of about 2:1. The binding energy of S $2p_{3/2}$ (163.3 eV) is lower than that of elemental S (164.0 eV), suggesting that the material suffers from the presence of weak C-S bonds. In addition, a broad peak of very low intensity exists near 167.1 eV because of the presence of partially oxidized

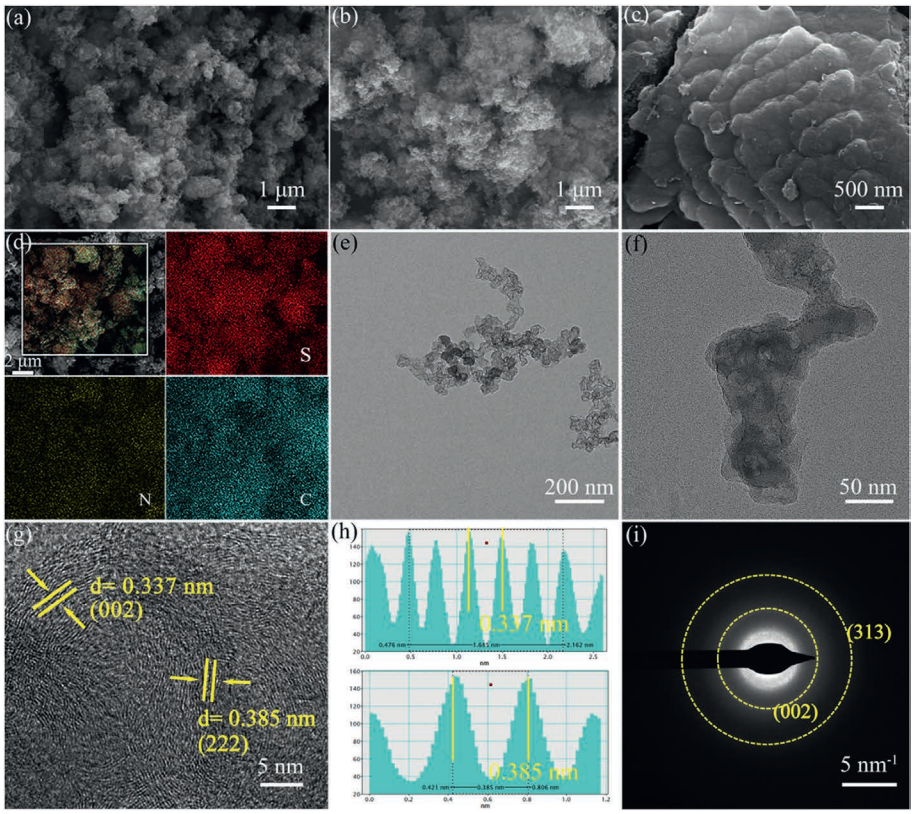


Fig. 2. Surface morphology and element distribution of different samples. SEM images of (a) S/KB, (b) S/KB-CN2 and (c) g-C_3N_4. (d) The corresponding mapping images of S/KB-CN2 sample. (e, f) TEM, (g) HRTEM, (h) Spacing value calculated from the corresponding phase profile, and (i) SAED of S/KB-CN2.

forms of sulfur. The XPS results further indicate the full binding and interaction of sulfur and g-C_3N_4.

Subsequently, Figs. 2a-d show the SEM images of S/KB, S/KB-CN2 and g-C_3N_4 as well as the elemental distribution of S/KB-CN2. The morphology of S/KB was found to be polymerized from primary particles with particle size of 40–50 nm (Fig. 2a). The S/KB-CN2 sample in Fig. 2b exhibits a similar microscopic morphology to the S/KB electrode, which suggests that the addition of g-C_3N_4 did not have an effect due to the smaller particle size of g-C_3N_4. The morphology of g-C_3N_4 in Fig. 2c is lamellar with uniform distribution. The particles loosely combined with each other, and have a large specific surface area, which can effectively adsorb polysulfides and facilitate the catalytic conversion of sulfur species. In addition, Fig. 2d illustrates the mapping of the S/KB-CN2 sample, from which it can be seen that all elements, including sulfur, carbon, and nitrogen, are uniformly distributed in the S/KB-CN2. This result verifies that g-C_3N_4 has successfully compounded with S/KB, and this composite has a high degree of homogeneity and purity.

To further characterize the structure and morphology of the material in depth, TEM and SAED of S/KB-CN2 were tested (Figs. 2e-i). The particle distribution in Fig. 2e is relatively uniform with a small amount of agglomeration. Some stacked particles can be observed in Fig. 2f, which are lamellar g-C_3N_4 distributed among them. Two lattice stripes of 0.337 nm and 0.385 nm can be clearly seen in the S/KB-CN2 composite (Fig. 2g), which correspond to the (002) crystal plane of g-C_3N_4 and the (222) crystal plane of S, respectively. The SAED plot in Fig. 2i shows the diffraction rings of S/KB-CN2, indicating that the composite is amorphous, which is consistent with previous findings. Then the spacing values for the phase profile analysis of the corresponding crystal planes (313) and (002) were calculated (Fig. 2h), which also corresponds to the XRD crystalline of S and g-C_3N_4 of the composite and indicates the successful compounding of materials.

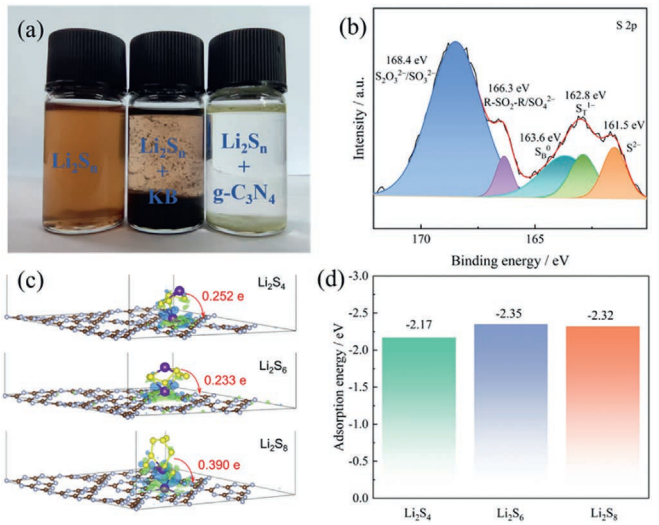


Fig. 3. Adsorbing ability of polysulfides on g-C_3N_4. (a) Visual adsorption experiment of different materials to polysulfides. (b) XPS spectra of S 2p for the g-C_3N_4 powder after soaked in polysulfide solution and then washed in the solvent repeatedly. (c) Adsorbing models of Li_2S_n ($n = 4$, 6 and 8) on g-C_3N_4 surface and (d) the corresponding adsorbing energy based on DFT calculations.

To better show the inhibition of the shuttling phenomenon of polysulfides, characterization of the adsorption effect is important (Fig. 3). First, a simple visual adsorption experiment was used to directly observe the adsorption effect of g-C_3N_4 on polysulfides (Fig. 3a). After 24 h of adding KB and g-C_3N_4 to the polysulfide solution, it was observed that the polysulfide solution with g-C_3N_4 was the lightest in color, indicating that g-C_3N_4 successfully ad-

sorbed the polysulfides, which is conducive to the inhibition of the "shuttle effect" in the reaction process of the battery. Then XPS spectra of the g-C_3N_4 powder after soaked in polysulfide solution and then washed in the solvent repeatedly was detected to determine the adsorption mechanism. Fig. S3a (Supporting information) shows the XPS full spectrum, which can be tested with S 2p, C 1s and N 1s. Fig. S3b (Supporting information) displays the XPS spectrum of N 1s and the fitting results, which are highly similar to those at the time of as-tested samples, with peaks of 398.5, 399.2, and 401.0 eV corresponding to the C-N=C, N-C_3, and -NH_x bonds, respectively. Then Fig. S3c (Supporting information) shows the XPS spectrum of C 1s, which corresponds to the g-C_3N_4 as is. Since there is no effect from the KB carbon source, the C-C at 284.6 eV is a result of the indeterminate source of carbon during the transfer process. The peaks at 286.1 and 288.9 eV correspond to C-O and C-N_3, respectively, which is consistent with that at the time of testing described above. Fig. 3b displays the XPS peaks and their fitting results for S 2p, which showed five fine peaks. The peaks at 168.4 eV and 166.3 eV correspond to $S_2O_3^{2-}$/SO_3^{2-} and R-SO_2-R/SO_4^{2-}, respectively, which are caused by oxidation of the sulfur species during the transfer and washing of the samples [29]. The three sub-peaks that appear in the low binding energy range include bridging sulfur (S_B^0) in polysulfides at 163.6 eV, terminal sulfur (S_T^{1-}) in polysulfides at 162.8 eV, and sulfur anion (S^{2-}) in Li_2S at 161.5 eV [30]. The above results further indicate the adsorption of g-C_3N_4 on polysulfide species.

In addition, to reveal the underlying mechanism of g-C_3N_4 to Li_2S_x ($x = 4$, 6, 8), the first principles calculations based on density functional theory (DFT) were performed. Calculations in Fig. 3c show that the adsorption of Li_2S_x on g-C_3N_4 results in a significant decrease in the specific electron density around the Li_2S_x molecule (blue region) and an enhancement of the electron density on the g-C_3N_4 substrate (green region). With the adsorption of polysulfides, the transfer of electrons from Li_2S_4, Li_2S_6, and Li_2S_8 to g-C_3N_4 are 0.252, 0.233, and 0.390 e, respectively. This suggests that the charge transfer between polysulfides and g-C_3N_4 is relatively easy during the redox process, and the smaller interfacial charge transfer resistance is favorable for the electrochemical properties of the material. Besides, when Li_2S_x was adsorbed on the g-C_3N_4 surface, the Li element in the Li_xS_y molecule showed a strong affinity with the double-coordinated N atoms in g-C_3N_4 (Fig. 3d), which made the Li_xS_y molecule more easily anchored to the g-C_3N_4 surface [31]. The calculated adsorption energies of Li_2S_4, Li_2S_6, and Li_2S_8 on g-C_3N_4 surface were −2.17, -2.35, and -2.32 eV, respectively, suggesting that the strong interactions between g-C_3N_4 and polysulfides contribute to the stabilization of the intermediates in the redox process. Thus, the "shuttle effect" of the cathode material is suppressed and the cycling stability of the cathode material will be improved.

To test the actual working effect in the battery, the kinetic characterization and the corresponding electrochemical performance of different samples were collected (Fig. 4). Then to explore the catalytic activity of g-C_3N_4, cyclic voltammetry (CV) tests were performed on the symmetric cells, while the carbon carrier KB in the sulfur-carbon composite was similarly subjected to CV tests for control. The corresponding cell structure is schematically shown in Fig. 4a. The symmetric cell consisted of an electrolyte containing Li_2S_6 and two identical g-C_3N_4/KB electrodes. Fig. 4b demonstrates the CV test results of KB and g-C_3N_4/KB symmetric cells. Two pairs of redox peaks can be roughly seen in the CV curves of g-C_3N_4/KB symmetric cell at ±0.46 and ±1.51 V, but the peaks are broad and overlapped, which cannot be clearly differentiated. However, the CV curves of KB symmetric cell do not show any obvious redox peaks [32]. This suggests that compared to KB, g-C_3N_4 can effectively promote the conversion of polysulfides. Fig. 4c shows the CV test used to investigate the redox process and electrochemical behavior of S/KB and S/KB-CN electrodes during the electrochemical reaction. The redox curves obtained from all the samples tested are highly similar, implying that the addition of g-C_3N_4 does not affect the electrochemical behavior of the original system of Li-S batteries. There are two distinct reduction peaks at around 2.44 and 2.0 V in the CV curves, which correspond to the reduction of sulfur to soluble long-chain polysulfides (Li_2S_x, $4 \le x \le 8$) and soluble polysulfides being further reduced to insoluble short-chain Li_2S_2 and Li_2S, respectively. The two reverse oxidation peaks at 2.31 V and 2.48 V show the opposite process, *i.e.*, the insoluble end products Li_2S_2 and Li_2S are oxidized to sulfur. The potential difference between the redox peaks of S/KB-CN2 is 0.305 V, which is much smaller than that of the other samples (0.333 V for S/KB, 0.331 V for S/KB-CN1, and 0.315 V for S/KB-CN3). This result suggests that the catalytic activity of moderate amount of g-C_3N_4 promotes the polysulfide conversion process and reduces the cell polarization, but too much catalyst affects the redox process. Moreover, the S/KB-CN2 sample exhibited higher current density and larger redox peak area than the other samples, which indicated that S/KB-CN2 had a higher reversible capacity.

Then, to further study the effect of g-C_3N_4 on the reaction kinetics of S/KB composites, electrochemical impedance spectroscopy (EIS) tests were performed. Fig. 4d shows the Nyquist plots of the S/KB and S/KB-CN samples, and all the curves contain semicircular regions and inclined straight-line regions. The high-frequency region presents a semicircle, and the two intercepts of the semicircle with the coordinate axis correspond to the ohmic resistance of the cell (R_s) and the charge transfer resistance between the electrolyte and the electrodes (R_{ct}), respectively. Fig. 4e displays the values of R_s and R_{ct} resulting from the impedance spectrum based on the equivalent circuit. The impedance of S/KB-CN2 ($R_s = 8.71\ \Omega$, $R_{ct} = 61.3\ \Omega$) is significantly smaller than that of S/KB ($R_s = 26.9\ \Omega$, $R_{ct} = 115\ \Omega$), S/KB-CN1 ($R_s = 8.84\ \Omega$, $R_{ct} = 76.7\ \Omega$) and S/KB-CN3 ($R_s = 10.9\ \Omega$, $R_{ct} = 84.4\ \Omega$), which indicates that the addition of appropriate amount g-C_3N_4 can significantly reduce the charge transfer resistance, promote the electron transfer at the interface and improve its reaction kinetics of lithium-sulfur batteries, but too much catalyst will likewise hinder the charge. In summary, S/KB-CN2 showed the best electrochemical kinetic activity. Then Fig. 4f demonstrates the charge-discharge curves for four samples (1.5-2.8 V, 1 C = 1600 mA/g). The shape of the curves for all the samples remains highly consistent and all the discharge curves have two plateaus. The first plateau at the initial stage of discharge is located at around 2.4 V, where S_8 is gradually reduced to Li_2S_4, a process known as solid-liquid conversion process. The second plateau in the discharge curve is located at 2.1 V, which corresponds to the conversion of Li_2S_4 to insoluble Li_2S_2 and Li_2S. Notably, the discharge capacity corresponding to the second plateau with the addition of g-C_3N_4 is significantly higher than that of the original sample. This is mainly attributed to the fact that g-C_3N_4 can adsorb long-chain polysulfides, which reduces the probability of polysulfide shuttling to a certain extent. Meanwhile, g-C_3N_4 catalyzes the conversion of long-chain polysulfides to short-chain, improves the utilization rate of dissolved polysulfide ions, and reduces the irreversible loss of active substances.

Subsequently, a galvanostatic intermittent titration technique (GITT) and rate performance was performed to further explore the practical kinetic enhancement of lithium-sulfur battery. For the GITT curves of the S/KB and S/KB-CN2 samples in Fig. S4 (Supporting information) and Fig. 4g, the black curve is the voltage-time curve, which is similar to the charging and discharging curves of the batteries, but it is a stepwise rise and fall due to the different test conditions. The GITT curves of the two samples were similar, implying that the addition of g-C_3N_4 did not affect the reaction process of the cell, and the reaction mechanism of the cell remained consistent. There are two discharge platforms at 2.4 V

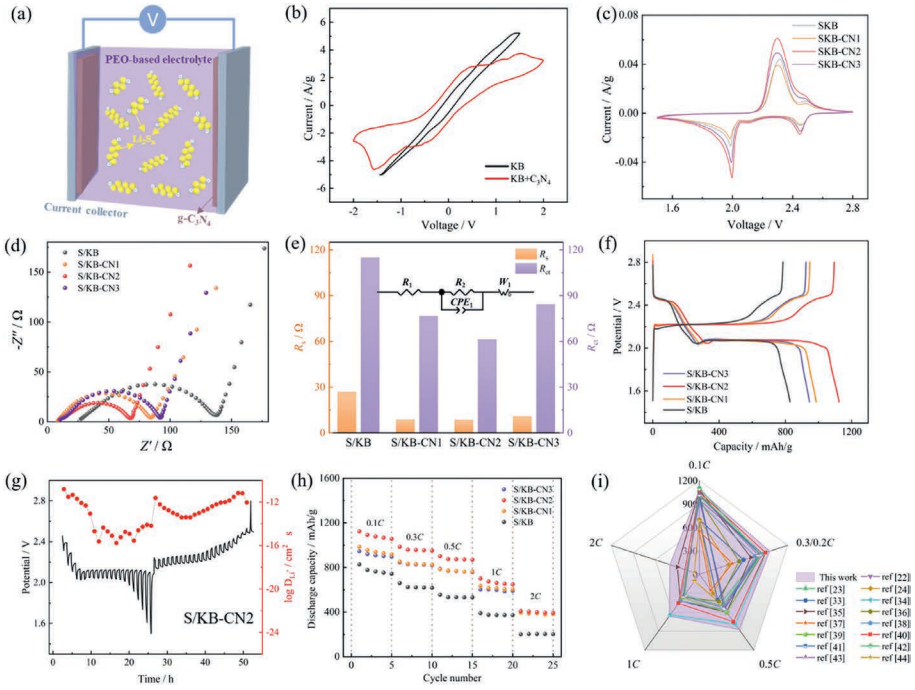


Fig. 4. Kinetic characterization and the corresponding electrochemical properties of different samples. (a) The schematic of a symmetric battery using two same electrodes coated with g-C_3N_4 and conversion of polysulfides. (b) Cyclic voltammograms of symmetric batteries with the electrodes of KB and g-C_3N_4/KB. (c) CV curves of the S/KB and S/KB-CN samples at 0.1 mV/s. (d) EIS results of the S/KB and S/KB-CN samples. (e) Fitting results of the S/KB and S/KB-CN samples and the corresponding equivalent circuit. (f) Charge-discharge curves of the S/KB and S/KB-CN samples. (g) Galvanostatic intermittent titration technique of S/KB-CN2 sample. (h) Rate performance of the S/KB and S/KB-CN samples. (i) Rate performance of Li–S batteries with PEO solid electrolyte.

and 2.0 V corresponding to the generation of long-chain polysulfides (Li_2S_x, $4 \leq x \leq 8$) and the transformation process to short-chain Li_2S_2 and Li_2S, respectively. The charging plateau, on the other hand, corresponds to the oxidation process, where the discharge end product is gradually oxidized to sulfur monomers, in agreement with the CV curve. The longer discharge time of S/KB-CN2 indicates that its discharge capacity is also higher. The red curve shows the diffusion coefficient as a function of time. Again, during the discharge process, the D values of S/KB-CN2 ranged from 3.16×10^{-16} to 1.58×10^{-11}, while those of S/KB ranged from 1.26×10^{-16} to 1.26×10^{-11}. Also, observation reveals that the D of S/KB-CN2 is greater than that of the S/KB electrode at almost all voltages, which is the same as the previous results of the electrochemical impedance. Hence, g-C_3N_4 incorporation improves the reaction kinetics and has a positive effect on the battery performance. Then the rate performance of S/KB and S/KB-CN were tested (Fig. 4h). The specific capacity of all electrodes decreases gradually with the increase of current density, which can be attributed to the polarization of the electrode materials at high current density. The specific initial discharge capacities of S/KB, S/KB-CN1, S/KB-CN2 and S/KB-CN3 are 828.18, 985.91, 1124.45 and 945.74 mAh/g, respectively. The first Coulomb efficiencies were 105.42 %, 104.01 %, 102.65 % and 102.27 %, respectively. The results showed that the addition of g-C_3N_4 could significantly improve the electrochemical performance of the battery. And the capacity of the electrodes with g-C_3N_4 was significantly increased at all rates compared to the unadded samples, indicating that the catalytic conversion of g-C_3N_4 improves the reaction kinetics of the lithium-sulfur batteries. S/KB-CN2 exhibits the highest specific capacity at 0.1, 0.3, 0.5, and 1 C, but when the current density is too high, the difference between S/KB-CN2 and S/KB-CN1 and S/KB-CN3 is not significant, but there is still a large enhancement compared to the original sample due to the limitation of the electron transfer at high current densities. Taken together, the catalysis of g-C_3N_4 facilitates the polysulfide conversion and thus improves the battery performance. Compared with previous studies [22–24,33–44], S/KB-CN2 materials show significantly improved rate performance (Fig. 4i).

To further elucidate the influence of g-C_3N_4 on S/KB, *in situ* EIS analyses were conducted on the S/KB-CN2 and S/KB samples. As illustrated in Figs. 5a and d, Figs. S5a and d (Supporting information), the S/KB-CN2 sample exhibited lower impedance and more stable Li^+ transport kinetics throughout the overall charge-discharge process compared to S/KB. The distribution of relaxation times (DRT) method was employed to visualize the results of the *in situ* EIS tests. According to Figs. 5b, c, e, and f, Figs. S5b, c, e and f (Supporting information), the regions corresponding to $\tau < 1$ and $\tau > 1$ are indicative of charge transfer reactions and Warburg diffusion processes, respectively. The impedance value distribution at different potentials correlates with the charge-discharge profiles of the materials. This further demonstrates that S/KB-CN2 exhibits reduced impedance during the overall charge-discharge process, indicating that the incorporation of g-C_3N_4 significantly enhances the Li^+ transport kinetics of the S/KB samples.

To verify the battery stability during cycling, the SEM and mapping images of S/KB and S/KB-CN2 samples before and after cycling (Figs. 6a-h) and the corresponding battery cycle stability (Fig. 6i) were measured. Obviously, the microstructure of the S/KB electrode showed significant changes with electrode broken and hollow, which is due to the destruction of the branched structure of KB during the cycling process. This structural change may reduce the conductivity and sulfur storage capacity of electrode, thus affecting the electrochemical property. In contrast, the microstructure of the S/KB-CN2 electrode appeared to be more intact with no obvious breakage or cavities after cycling, which is because the presence of g-C_3N_4 can improve the structural stability of the electrode material during cycling. Meanwhile, more uniform sulfur distribution on the S/KB-CN2 electrode was found by mapping

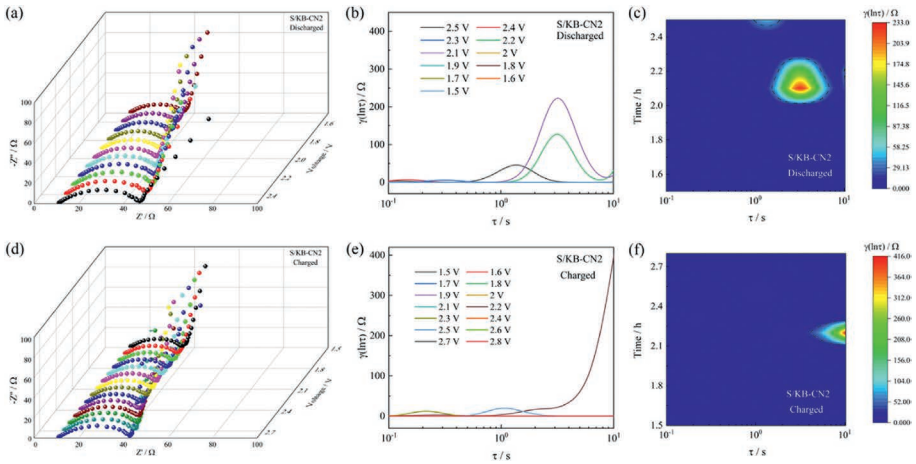


Fig. 5. Kinetic analysis of S/KB-CN2 samples. *In situ* EIS and corresponding DRT transformation for S/KB-CN2 samples at (a-c) discharge and (d-f) charge.

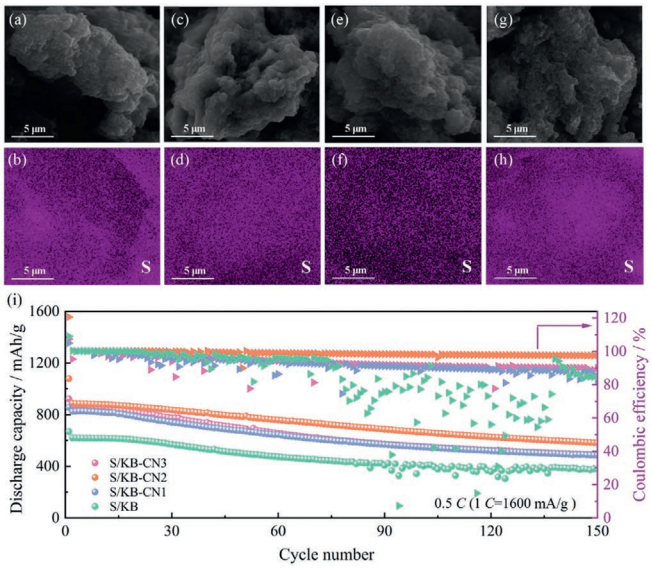


Fig. 6. SEM and mapping images of S/KB and S/KB-CN2 samples before and after cycling and the corresponding cycling stability. (a, b) S/KB before cycling, (c, d) S/KB after cycling, (e, f) S/KB-CN2 before cycling, and (g, h) S/KB-CN2 after cycling. (i) Cycling stability of S/KB and S/KB-CN2 samples.

plots. In addition, it can be found from Fig. S6 (Supporting information) that the N element is evenly distributed before and after the cycle. This further confirms that g-C_3N_4 has a good adsorption effect on polysulfides and can maintain stability during the cycle, which can help immobilize sulfur on the electrodes and prevent it from leaching out of the electrodes, thus improving the cycling stability. Then Fig. 6i demonstrates the cycling performance of S/KB with S/KB-CN samples at 0.5 C. The capacity is abnormally high in the first cycle because of the presence of side reactions. From the second cycle, S/KB, S/KB-CN1, S/KB-CN2, and S/KB-CN3 achieve discharge capacities of 619.8, 824.9, 887.9 and 867.4 mAh/g, respectively. After 150 cycles, the four samples can provide discharge capacities of 377.1, 486.1, 582.2 and 489.7 mAh/g, respectively, suggesting that the S/KB-CN2 possess the highest capacity with the retention of 65.57 %, while the capacity retention rate of S/KB is only 60.84 %. Besides, the Coulombic efficiency can be visualized as a "shuttle effect". The S/KB has the worst result with the Coulombic efficiency gradually decreasing from 30 cycles to a minimum of 71.43 %, implying a severe overcharging phenomenon arising from polysulfides diffusion. The Coulombic efficiencies of S/KB-CN1 and S/KB-CN3 were relatively stable, but gradually increased to 88.03 % and 88.81 % after 150 cycles with a slight "shuttle effect". The Coulombic efficiency of the S/KB-CN2 sample finally reached 97.47 %, which was the best among the four samples. The reason is that g-C_3N_4, as a catalyst, can effectively adsorb polysulfides on the cathode side, catalyze their transformation, accelerate the redox reaction, and inhibit the "shuttle effect", whereas the addition of too much catalyst reduces the ratio of the active substance to the polysulfides and prevents the diffusion of polysulfides, which reduces the specific capacity. The specific capacity of S/KB-CN3 is lower than that of S/KB-CN2, which suggests that 5 wt% of g-C_3N_4 is the optimal composite amount. Subsequently, to further investigate the efficiency during the reaction process, charge-discharge curves of S/KB and S/KB-CN samples at various cycles of 0.5 C and different rates were exhibited (Fig. S7 in Supporting information). Notably, the charging capacity is larger than the discharging capacity in all samples except S/KB-CN2 at 30 cycles, and a "shuttle effect" occurs, while the capacity decay rate starts to accelerate. The Coulombic efficiency of the S/KB-CN2 sample was around 100 % in the first 100 cycles and only 2.6 % lower after 150 cycles while being very stable. During different rates, the curve trends were similar for each sample, with the plateau gradually decreasing until disappearing near 2.2 V and decreasing near 2.0 V. The discharge capacities of the S/KB-CN2 electrode at 0.1, 0.3, 0.5, 1, and 2 C were 1078.5, 959.6, 874.9, 701.1 and 393.0 mAh/g, respectively. The S/KB-CN2 electrode was the highest at the same current density, S/KB-CN2 electrodes all have the highest discharge specific capacity at the same current density, while S/KB has the lowest discharge capacity. It was further demonstrated that g-C_3N_4 could improve the electrochemical performance.

In summary, this work proposed an innovative concept of adsorption and catalysis into polymer ASSLSBs. The XRD, XPS, SEM and TEM confirms that g-C_3N_4 has been successfully complexed with S/KB with high integrity and purity. Simple and intuitive visualization experiments as well as calculations successfully demonstrated that g-C_3N_4 has strong adsorption properties for polysulfides. The redox peaks in the CV curves of the symmetric cell indicates that g-C_3N_4 has obvious electrocatalytic ability for polysulfides conversion, which can effectively promote the conversion of soluble long-chain polysulfides to the final product. The g-C_3N_4's adsorption and catalytic properties can effectively inhibit polysulfide shuttling, improve sulfur utilization, and accelerate the kinetics of the cell reaction. *In situ* EIS test further verified that g-C_3N_4 enhanced the Li^+ transport dynamics. Among the differ-

ent ratios of g-C_3N_4, the S/KB-CN2 sample shows higher current density, larger redox peak area and smaller charge transfer resistance than the other samples, which suggests that S/KB-CN2 has a larger reversible capacity and better dynamic properties than the other materials. Finally, the S/KB-CN2 electrode had the highest discharge capacity of at 1078.5 mAh/g (0.1 C), 959.6 mAh/g (0.3 C), 874.9 mAh/g (0.5 C), 701.1 mAh/g (1 C), and 393.0 mAh/g (2 C), respectively. The discharge capacity of the S/KB-CN2 sample could achieve 582.2 mAh/g with a capacity retention of 65.6 % and a Coulombic efficiency of 97.47 % after 150 cycles at 0.5 C, which is the best performance of all samples. In addition, the average Coulomb efficiencies of S/KB, S/KB-CN1, S/KB-CN2, and S/KB-CN3 were 73.69 %, 91.83 %, 98.72 %, and 93.11 % after 150 cycles, which indicated that g-C_3N_4 could accelerate the reaction kinetics and inhibit the "shuttle effect".

Declaration of competing interest

The authors declare that they have no known competing financial interests or personal relationships that could have appeared to influence the work reported in this paper.

CRediT authorship contribution statement

Ying Li: Writing – original draft, Methodology, Formal analysis. **Ze-Chen Lv:** Writing – review & editing, Data curation. **Peng-Fei Wang:** Writing – review & editing, Supervision, Project administration. **Jie Shu:** Writing – review & editing, Supervision. **Ping He:** Writing – review & editing, Supervision. **Ting-Feng Yi:** Writing – review & editing, Supervision, Project administration, Funding acquisition.

Acknowledgments

This work was supported by the National Natural Science Foundation of China (Nos. 22309027 and 52374301), the Natural Science Foundation of Hebei Province (No. E2024501010), the Shijiazhuang Basic Research Project (Nos. 241790667A and 241790907A), the Fundamental Research Funds for the Central Universities (Nos. N2423054 and N2423052), the Performance subsidy fund for Key Laboratory of Dielectric and Electrolyte Functional Material Hebei Province (No. 22567627H).

Supplementary materials

Supplementary material associated with this article can be found, in the online version, at doi:10.1016/j.cclet.2025.111110.

References

[1] G. Zhu, X. Tian, H.C. Tai, et al., Nature 596 (2021) 525–530.
[2] C.Y. Wang, T. Liu, X.G. Yang, et al., Nature 611 (2022) 485–490.
[3] S.B. Yang, B. Wang, Q. Lv, et al., Chin. Chem. Lett. 34 (2023) 107783.
[4] J. Zhou, M.L. Holekevi Chandrappa, S. Tan, et al., Nature 627 (2024) 301–305.
[5] Y. Wang, H.X. Chen, F.D. Yu, et al., Chin. Chem. Lett. 35 (2024) 109001.
[6] S. Zhou, J. Shi, S. Liu, et al., Nature 621 (2023) 75–81.
[7] Y.C. Ji, K. Yang, M.Q. Liu, et al., Adv. Funct. Mater. 31 (2021) 2104830.
[8] H.H. Duan, L.P. Liao, R. Bi, et al., J. Mater. Chem. A 11 (2023) 19046–19055.
[9] H.H. Duan, J.H. Liu, J.F. He, et al., J. Energy Chem. 98 (2024) 87–95.
[10] L. Schweiger, K. Hogrefe, B. Gadermaier, et al., J. Am. Chem. Soc. 144 (2022) 9597–9609.
[11] P.F. Wang, X. He, Z.C. Lv, et al., Adv. Funct. Mater. 33 (2023) 2211074.
[12] D. Zhou, D. Shanmukaraj, A. Tkacheva, et al., Chem 5 (2019) 2326–2352.
[13] Q. Zhao, S. Stalin, C.Z. Zhao, et al., Nat. Rev. Mater. 5 (2020) 229–252.
[14] J. Yin, X. Xu, S. Jiang, et al., Chem. Eng. J. 431 (2022) 133352.
[15] D. Wang, L.J. Jhang, R. Kou, et al., Nat. Commun. 14 (2023) 1895.
[16] P.F. Wang, Y.H. Zhao, S.-H. Tian, et al., Energy Fuels 37 (2023) 15198–15205.
[17] H.H. Duan, L.S. Li, X.X. Fu, et al., Chem. Eng. J. 450 (2022) 138208.
[18] J. Li, F. Xie, W. Pang, et al., Sci. Adv. 10 (2024) 3925.
[19] F. Lee, M.C. Tsai, M.-H. Lin, et al., J. Mater. Chem. A 5 (2017) 6708–6715.
[20] F. Wu, K. Zhang, Y. Liu, et al., Energy Storage Mater. 33 (2020) 26–54.
[21] X. Tao, Y. Liu, W. Liu, et al., Nano Lett. 17 (2017) 2967–2972.
[22] H. Zhang, X. Judez, A. Santiago, et al., Adv. Energy Mater. 9 (2019) 1900763.
[23] G.G. Eshetu, X. Judez, C. Li, et al., J. Am. Chem. Soc. 140 (2018) 9921–9933.
[24] H. Zhang, U. Oteo, X. Judez, et al., Joule 3 (2019) 1689–1702.
[25] J. Wang, S. Wang, Coord. Chem. Rev. 453 (2022) 214338.
[26] D. Yuan, Y. Dou, Z. Wu, et al., Chem. Rev. 122 (2022) 957–999.
[27] P.F. Wang, Y. Li, S.H. Tian, et al., Energy Fuels 37 (2023) 15170–15178.
[28] S. Zhang, N. Zhong, X. Zhou, et al., Nano-Micro Lett. 12 (2020) 112.
[29] Y. Wu, T. Momma, S. Ahn, et al., J. Power Sources 366 (2017) 65–71.
[30] Z. Jin, T. Lin, H. Jia, et al., ACS Nano 15 (2021) 7318–7327.
[31] Y. Sun, W. Huang, J. Li, et al., AIChE J. 69 (2023) e17940.
[32] B. Al Alwan, Z. Wang, W. Fawaz, et al., Energies 15 (2022) 15217827.
[33] X. Judez, H. Zhang, C. Li, et al., J. Phys. Chem. Lett. 8 (2017) 1956–1960.
[34] Y. Wang, S. Geng, G. Yan, et al., J. Am. Chem. Soc. 5 (2022) 2495–2504.
[35] C. Fan, W. Meng, J. Han, et al., Energy Storage Mater. 71 (2024) 103554.
[36] Y. Wang, G. Wang, P. He, et al., Chem. Eng. J. 393 (2020) 124705.
[37] A. Chatterjee, D. Ganguly, R. Sundara, et al., Energy Technol 12 (2024) 2300576.
[38] H. Cheng, C. Yan, L. Chang, et al., ACS Appl. Energy Mater. 7 (2024) 3071–3081.
[39] B. Hu, S. Han, J. Zhang, et al., J. Colloid Interface Sci. 650 (2023) 203–210.
[40] J. Sheng, Q. Zhang, C. Sun, et al., Adv. Funct. Mater. 32 (2022) 2203272.
[41] H. Duan, L. Liao, R. Bi, et al., J. Mater. Chem. A 11 (2023) 19046–19055.
[42] Z. Ao, H. Li, Y. Zou, et al., Acta Mater. 270 (2024) 119880.
[43] J.T. Lee, M.C. Lin, C.M. Leu, et al., J. Mater. Chem. A 10 (2022) 12928–12937.
[44] Z.C. Li, T.Y. Li, Y.R. Deng, et al., Rare Met. 41 (2022) 2834–2843.